Epitaxial columnar growth of strain-free antiferromagnetic Weyl semimetal Mn_3Sn on wurtzite c-plane $GaN/Al_2O_3(0001)$

Hannah Hall, Sunil Timilsina, Sneha Upadhyay, Tyler Erickson,
Cherie D'Mello, David C. Ingram, and Arthur R. Smith[a]

[1]*Nanoscale and Quantum Phenomena Institute,*
Department of Physics and Astronomy,
Ohio University, Athens, OH 45701, USA

(Dated: November 8, 2025)

Abstract

Weyl semimetal thin films with excellent crystalline quality are of great interest for antiferromagnetic spintronics. Mn_3Sn is one Weyl semimetal with great properties and promise for exciting science and applications. It has proven very challenging, however, to grow Mn_3Sn thin films with smooth surfaces, negligible strain, and excellent crystallinity. In this work, we discuss the successful preparation of epitaxial Mn_3Sn (0001)-oriented thin films via molecular beam epitaxial growth on c-plane wurtzite GaN which was grown by MBE on Al_2O_3 (0001). We present the reflection high energy electron diffraction analysis along with x-ray diffraction in order to demonstrate the crystalline quality of the film, and we give atomic models to explain the epitaxial orientation relationships between the crystal lattices of the substrate, GaN layer, and Mn_3Sn layer. Importantly, we discuss the film lattice parameters as compared to expected values, demonstrating negligible strain both *in-plane* and *out-of-plane*. Atomic force microscopy reveals an epitaxial columnar growth mode characterized by flat-top-mesa islands, while scanning tunneling microscopy shows the atomically smooth surfaces of the mesa-top structures. Finally, Rutherford backscattering informs the stoichiometry of the film as well as the layer thicknesses.

Keywords: Weyl semimetal, chiral antiferromagnetic material, spintronics, molecular beam epitaxy, reflection high energy electron diffraction, scanning tunneling microscopy

[a] Corresponding Author : smitha2@ohio.edu

I. INTRODUCTION

There has been intensive interest in the spintronic applications of Weyl semimetal Mn_3Sn owing to its chiral antiferromagnetic properties while at the same time having a tiny, residual magnetic moment which is affected by strain. Multiple Weyl points near the Fermi level as well as resultant Fermi arcs at the surface were theoretically predicted by Yang *et al.*[1] Experimentally, there have been observations of large anomalous Hall effect at room temperature,[2, 3], anomalous Nernst effect, magneto-optical Kerr effect, and magnetic spin-Hall effect.[4–6] Even exchange bias has been reported.[7] What makes Mn_3Sn so interesting for spintronics is not that these effects can be seen in an antiferromagnetic semimetal, but that they can be seen at very small applied magnetic field owing to its very weak and soft octupole moment.[2, 8] Impressively, Higo *et al.* reported the use of perpendicular spin current to fully switch the magnetic octupole moment (with all Mn spins flipping in the process) for a 30 nm-thick Mn_3Sn thin film by spin-orbit torque, but critical to achieve a net octupole moment was the presence of 0.2 % tensile strain along $11\bar{2}0$ (ascribed to substrate lattice mismatch) which was enough to induce perpendicular magnetic anisotropy of the octupole moment.[9] Yoon *et al.* further discuss the spin-orbit torque switching of the octupole moment in terms of a handedness anomaly.[10] In all cases of interest, it is important to quantify the material quality, strain of the thin film, and surface properties. A lot of efforts have been made to fabricate thin films with excellent and controlled phase purity, crystallinity, orientation, and strain. In fact, strain in Mn_3Sn is a material property which is being used to engineer the spintronic device properties.[9–11]

Different methods and substrates have been used to grow Mn_3Sn including both MBE and sputtering on Al_2O_3 and MgO. In our previous work, we used molecular beam epitaxy in order to grow Mn_3Sn thin films on Al_2O_3 (0001) substrates, and we reported two qualitatively different results. In one case, we observed the growth of mainly *c*-plane oriented Mn_3Sn (0001) with low strain,[12] while in the other, under different conditions we observed growth of *a*-plane oriented Mn_3Sn with large amounts of strain.[13] In both cases, the growth involved both a deposition step and a time delay step (to allow the film time to crystallize). In fact, the large mismatch (+19.0%) between a_{Mn3Sn} (5.665 Å)[4] and a_{Al2O3} (4.759 Å)[14, 15] could be one reason for the difficulty in growing smooth epitaxial Mn_3Sn films on this substrate. As such, finding a more ideal substrate is desirable. One possibly better candidate is c-plane GaN. A c-plane GaN substrate, besides having a lattice mismatch (after 30° axis rotation) of only +2.63%, could have the added advantage of combining a wide band-gap semiconductor with an antiferromagnetic Weyl semimetal for spintronics applications.

In this work, we report the successful growth of Mn_3Sn (0001) with excellent film and surface quality on c-plane wurtzite GaN as grown on c-plane Al_2O_3. We review first the growth of c-plane GaN on Al_2O_3 (0001) and then introduce the growth of Mn_3Sn on c-plane GaN.

II. METHODOLOGY

The growth of Mn_3Sn thin films was performed using a custom-designed molecular beam epitaxy (MBE) system equipped with a radio-frequency (RF) plasma source supplied with 6N ultra-high purity nitrogen gas (N_2) and knudsen-type effusion cells filled with 4N purity manganese (Mn), 5N purity tin, and 6N purity gallium, with precise temperature control maintained by Eurotherm 2416 controllers. Real-time monitoring of surface structural evolution was conducted using a reflection high-energy electron diffraction (RHEED) system (KSA 400). In RHEED, the observed diffraction pattern is directly linked to the surface crystallography of the sample, particularly the *in-plane* periodicity of lattice points. For hexagonal crystal structures, the RHEED pattern provides insightful information when the electron beam is aligned along specific azimuthal directions. Two commonly studied azimuths are the $[11\bar{2}0]$ (a-axis) and the $[10\bar{1}0]$ (m-axis). These directions correspond to 0° and 30° orientations of the incident electron beam with respect to the hexagonal high symmetry axis.

Source flux calibration and thickness monitoring were performed using a quartz crystal microbalance (QCM - Inficon STM-2). The base pressure in the MBE growth chamber was maintained at 5.8×10^{-9} Torr. Basal (c)-plane sapphire (Al_2O_3) substrates (MTI Corporation, 10 mm × 10 mm × 0.5 mm, single-side polished) were back-coated by titanium and then cleaned *ex-situ* using acetone and isopropanol, followed by *in-situ* annealing at 770 °C for ∼1 hour under active N_2 plasma at a chamber pressure of 2.0×10^{-5} Torr to nitridate the surface prior to GaN and Mn_3Sn deposition.

A GaN buffer layer was deposited at ∼498°C using a Ga flux of 3.14×10^{14}/cm^2/s, establishing a Ga:N flux ratio of ∼1:1. Following buffer layer growth, the substrate temperature was increased to ∼660°C for the deposition of the main GaN layer, which was grown for approximately 50 min to achieve a thickness of ∼200 nm. To remove residual surface Ga adatoms prior to Mn_3Sn deposition, the substrate was annealed at ∼851°C for 90 min. The Mn and Sn effusion cell temperatures were adjusted to achieve fluxes of $2.63\times10^{14}/cm^2/s$ and $7.30\times10^{13}/cm^2/s$, respectively, establishing a Mn:Sn atomic flux ratio of ∼3:1. The substrate temperature was then reduced to ∼300°C for Mn_3Sn growth, during which both Mn and Sn shutters were opened simultaneously for ∼70 min, resulting in a film thickness of ∼ 200 nm.

Post-growth structural analysis was performed *ex-situ* using high-resolution X-ray diffraction (XRD) on a Rigaku MiniFlex II benchtop XRD system. The resultant spectrum was calibrated from the sapphire (0001) substrate peak. Peak fitting was performed using Pseudo-Voigt fitting functions in order to extract best peak positions and peak widths.

To obtain chemical composition, Rutherford backscattering spectrometry (RBS) was performed on the sample using the 4.5 MV tandem Van de Graaf accelerator in the Edwards Accelerator Laboratory at Ohio University. Because of the masses involved in this sample - Ga, Mn, and Sn - various energies were tried to find one at which the three peaks could be resolved as separate peaks. This occurred at 5.5 MeV (incident 4He++ particle beam energy) scattered through an angle of 168°. To avoid channeling, the sample was oriented with its surface normal at 7.5° relative to the incident beam and with the sample rotated on the sample holder about 20° so that the major planes of the sample were not in the vertical or horizontal relative to the beam. RBS was also performed at 2.2 MeV in order to compare to the simulated spectrum from RUMP.[16]

Atomic force microscopy (AFM) measurements were performed using a ThermoMicroscopes Autoprobe CP research AFM system under ambient conditions. The cantilever oscillated near its resonant frequency of 320 kHz and interacted with the sample surface through Van der Waals forces, with deflections detected via a laser beam reflected into a photodiode. Variations in the reflected signal were converted into high-resolution surface topography. Image flattening and quantitative morphological analyses were performed using the WSxM software.[17]

III. EXPERIMENTAL RESULTS

A. Wurtzite GaN ($000\bar{1}$) growth on sapphire (0001)

The lattice mismatch between wurtzite GaN($000\bar{1}$) and basal plane Al_2O_3 (0001) is well known, as illustrated in Fig. 1(a), clearly showing the poor lattice matching when the two materials have their crystalline [$11\bar{2}0$] axes aligned. Nevertheless, Al_2O_3(0001) (also known as corundum), with lattice constants a = 4.759 Å and c = 12.992 Å,[14, 15] serves as a widely adopted substrate for III-nitride heteroepitaxy owing to its high thermal stability, chemical inertness, and ready commercial availability. The basal plane of sapphire presents a hexagonal-like, but distorted, close-packed arrangement of O sublattice atoms, with 1×1 unit cell Al lattice points represented in Fig. 1(a) by large red-filled circles exhibiting 6-fold rotational symmetry about the [0001] axis (Note: the Al atoms of Al_2O_3 are arranged in a rhombohedral pattern within the hexagonal framework, resulting in a periodic distortion which repeats every 6 layers along the c-axis).[18, 19] In fact, due to the rhombohedral structure, the nearest neighbor oxygen spacing in the bulk is just $\sim$ 2.748 Å, and the hexagonal-like O sublattice (gray-filled circles) is actually 30°-rotated relative to the sapphire unit cell lattice, as can be seen by comparing the red-fill circles hexagon with the gray-filled circles hexagon.[20] Overlaid on the Al_2O_3 (0001) surface lattice is the c-plane GaN 1×1 unit cell lattice ($a = 3.189$ Å, $c = 5.185$ Å), shown as smaller solid blue circles and having a ($000\bar{1}$)-polar Ga surface termination with triangular lattice symmetry. *In-plane* crystallographic alignment between the Al_2O_3 and GaN lattices is indicated by their parallel red and blue direction vectors, respectively; for example, in this alignment, [$11\bar{2}0$] of Al_2O_3 $\parallel$ [$11\bar{2}0$] of GaN. In this case, there would be a large lattice mismatch of -33% between the GaN and sapphire lattices. This mismatched alignment, if it occurred, would result in large interfacial strain and would be energetically unfavorable.

The large mismatch problem can be partially solved if the crystalline axes of GaN are rotated 30° about the Al_2O_3 [0001] axis as illustrated in Fig. 1(b). In this case, the [$11\bar{2}0$] of GaN is now aligned with the [$10\bar{1}0$] of Al_2O_3, and the [$1\bar{1}00$] of GaN is now aligned with the [$1\bar{2}10$] of Al_2O_3 (Note: in the hexagonal Miller-Bravais index system, [$1\bar{1}00$] $\perp$ [$11\bar{2}0$] whereas [$10\bar{1}0$] $\angle 30°$ [$11\bar{2}0$]). The advantage of doing this is seen in that the lattice spacing for GaN is now much more closely matched to the lattice spacing of Al_2O_3, and this advantage was emphasized in early GaN on sapphire growth papers.[21] Numerically, this works out to equal (5.52 - 4.759)/4.759 = +16.0% lattice mismatch. Therefore, the mismatch is reduced (in magnitude) by a factor of 2×, from −33.2% to +16.0%, while the strain switches sign from tensile (negative strain) to compressive (positive strain). That this occurs upon GaN growth on Al_2O_3 (0001) is clearly seen in the RHEED patterns shown in Fig. 1(d-g). Here, Fig. 1(d,e) show RHEED patterns for Al_2O_3 (0001), while Fig. 1(f,g) show RHEED patterns for GaN. We can see that the $\langle 11\bar{2}0\rangle$ and $\langle 10\bar{1}0\rangle$ crystal vector directions interchange going from Al_2O_3 to GaN. For example, the streak spacing ratio (1:$\sqrt{3}$) for $\langle 11\bar{2}0\rangle$ relative to $\langle 10\bar{1}0\rangle$ becomes ($\sqrt{3}$:1) between Figs. 1(d,e) (Al_2O_3) and Figs. 1(f,g) (GaN).

It has been well understood that the lattice mismatch problem is further reduced by nitridation of the Al_2O_3 (0001) substrate surface prior to GaN growth, for example using a radio frequency (RF) activated nitrogen plasma source (RF N-plasma). And the advantages of nitridation for substrate preparation for GaN growth has been well discussed in the literature.[22–26] Heinlein *et al.* and others have discussed that plasma pre-conditioning of the sapphire surface results in the formation of a surface nitride.[24] One of the earliest reports of Al_2O_3 nitridation was by Kawakami *et al.* who used NH_3 gas to nitridate the surface at 1200 °C prior to AlN growth with flat surface and good crystallinity.[27] Formation of an AlN-like surface layer can be accomplished by substituting N atoms for O atoms in the first layer, and the N atoms bonding with both 1st and 2nd layer Al atoms. This is shown in Fig. 1(c) where the AlN surface unit cell vectors lie at 30° with respect to Al_2O_3 and with increased atomic spacing, going from O-O distances of $\sim$ 2.75 Å to N-N (and Al-Al) distances closer to 3.11 Å.

The increased effective lattice constant may be attributed to the larger atomic radius of nitrogen (56 pm) relative to that of oxygen (48 pm), creating compressive strain within the surface. But it may also be related to the tetrahedral bonding favored by N atoms versus the octahedral bonding favored by O atoms. The increased *in-plane* lattice spacing is directly observed in the RHEED pattern shown in Fig. 1(d) by the fact that the streaks are unevenly spaced. This uneven spacing is an indication that the surface has been nitridated.

It is interesting to note a recent paper by Hütner *et al.* who present atomic resolution images of high-temperature-annealed sapphire (0001) by means of atomic-resolution (qPlus force sensor AFM) studies and combine that with computational modeling (density functional theory with machine learning).[28] They argue that the high-temperature-annealed sapphire (0001) surface, which reconstructs upon annealing in vacuum (to $\sim 1000°$ or higher) to a more energetically favorable $\sqrt{31} \times \sqrt{31})R\pm 9°$ structure, is stabilized by increasing Al coordination at the surface. They model the surface layer as being slightly oxygen deficient (as compared to bulk) with an average surface Al-Al spacing of ~ 3.04 Å,[28] and surface O-O neighbors share the same, or in some cases smaller, spacing. However, the high temperature annealing conditions are quite different compared to the plasma nitridation used in our study, and with the nitridated surface we do not observe the complex RHEED pattern seen for the $\sqrt{31} \times \sqrt{31})R\pm 9°$ reconstruction as seen by Smink *et al.*;[29] instead, our nitridated Al_2O_3 (0001) surface has just a 1×1 structure.

A careful RHEED pattern analysis for the nitridated Al_2O_3 surface and the overgrown GaN surface are shown in Fig. 2. As shown in Fig. 2(a) and 2(b), the original Al_2O_3 streaks are still visible for both azimuths. Upon high-temperature (770 °C) annealing plus nitridation of the sapphire substrate, an epitaxial AlN-like buffer layer is formed, as evidenced by the emergence of new first-order RHEED streaks marked with cyan dashed lines Fig. 2(a-b). The Al_2O_3 streaks are indicated by the red dashed lines and labels, while the AlN-like streaks are indicated by the cyan dashed lines and labels. The streak spacings are given in terms of multiples of the reciprocal lattice spacings from fundamental formulas. The Al_2O_3 [11$\bar{2}$0:10$\bar{1}$0] streak spacing ratio is 1:$\sqrt{3}$, but the AlN-like streaks spacing ratio is inverted to become $\sqrt{3}$: 1. This inversion of streak spacing, when viewed in the same crystallographic reference frame of the sapphire, directly indicates a 30° *in-plane* rotation of the AlN epilayer relative to the sapphire crystalline lattice. And we conclude that the nitridated surface has an effective (diagonal) lattice constant close to 5.272 Å and that the surface has become AlN-like with a lattice spacing of 3.044 ± 0.028 Å, not far from the value recently reported by Nilsson *et al.* for homoepitaxial AlN layers grown by metalorganic chemical vapor deposition at high temperatures, $a_{AlN} = 3.11131 \pm 0.00016$ Å.[30]

The result is a nitridated substrate with a lattice mismatch of only $\sim -4.55\%$ with respect to the GaN reported lattice constant (3.189 Å). GaN growth on the nitridated Al_2O_3 (0001) proceeded under optimized conditions. The resulting RHEED streaks, marked by the dashed and labeled streaks in Fig. 2(c,d), are slightly closer together than those of the nitridated AlN-like lines, indicating coherent epitaxial growth with the same *in-plane* rotational alignment and resulting, for the thick layer of GaN, in a lattice constant $a = 3.180 \pm 0.008$ Å, in excellent agreement with the accepted value ($a = 3.189$ Å). Collectively, these results demonstrate the critical role of high-temperature annealing plus nitridation of the Al_2O_3 substrate surface plus the *in-plane* 30° lattice rotation in accommodating lattice mismatch and enabling high-quality GaN heteroepitaxy.

B. Weyl semimetal Mn_3Sn epitaxial growth on Wurtzite GaN

Figure 3 presents a comparative lattice analysis illustrating possible epitaxial alignments between kagome $Mn_3Sn(0001)$ and wurtzite $GaN(000\bar{1})$. In the simple triangle-on-triangle configuration seen in Fig. 3(a), the hexagonal Mn_3Sn lattice ($a = 5.665$ Å), represented by an array of large magenta circles, is aligned on top of the wurtzite GaN lattice ($a = 3.189$ Å), represented by an array of smaller solid blue circles; here, Mn_3Sn $[11\bar{2}0] \parallel$ GaN $[11\bar{2}0]$. However, this simple alignment would have an epitaxial lattice mismatch of approximately -11.2%, and if it was accommodated by elastic strain, there would be large elastic tensile strain which would be energetically unfavorable.

In exactly the same way that the mismatch is reduced for GaN on Al_2O_3 (0001) by a 30° lattice rotation, the mismatch between $Mn_3Sn(0001)$ and GaN $(000\bar{1}]$ is reduced by rotating the Mn_3Sn lattice 30° *in-plane*, as shown in Fig. 3(b), in which the $[11\bar{2}0]$ direction of Mn_3Sn is now aligned with the $[10\bar{1}0]$ direction of GaN. In this orientation, Mn atoms (green dots) in the kagome lattice at the ideal interface are located at bridge sites of the Ga lattice (blue dots) of the last GaN bilayer. This rotated alignment is shown by the magenta and blue direction vectors, where the $[11\bar{2}0]$ of Mn_3Sn is rotated 30° with respect to the $[11\bar{2}0]$ of GaN. Given the hexagonal symmetry, this rotation matches the a-spacing of Mn_3Sn (5.665 Å) with the $\sqrt{3}a$ spacing of GaN (5.524 Å), reducing the *in-plane* lattice mismatch to (5.665-5.524 Å)/5.524 Å= +2.63%. This rotational alignment significantly improves lattice match and is anticipated to reduce interfacial strain energy.

The diagram shown in Fig. 3(c) illustrates the epitaxial alignment anticipated for the full heterostructure stack, consisting of $Mn_3Sn(0001)/GaN(000\bar{1})/Al_2O_3$ (0001). Since the Mn_3Sn lattice is rotated 30° to the GaN lattice and the GaN lattice is rotated 30° to the Al_2O_3 lattice, the Mn_3Sn lattice is aligned with the underlying Al_2O_3 lattice. To show that this definitely occurs during growth, Fig. 4 presents the evolution of the RHEED streak patterns acquired during the entire epitaxial growth process for Mn_3Sn/c-plane GaN/c-plane Al_2O_3. The left and right panels correspond to the sapphire $[11\bar{2}0]$ and $[10\bar{1}0]$ azimuths, respectively, probed using the 0° and 30° incident electron beam directions.

RHEED streak images of the nitridated Al_2O_3 substrate shown in Figs. 4(a,b) display sharp streaks characteristic of a well-ordered surface. As mentioned, the 30° crystalline rotation is already present after the nitridation, and the GaN growth shown in Figs. 4(c,d) maintains crystalline alignment with the rotated AlN-like lattice of the nitridated Al_2O_3 surface. Just after opening the Mn and Sn shutters, nucleation of the Mn_3Sn lattice occurs, with the RHEED patterns shown in Figs. 4(e,f)) exhibiting emerging streaky + spotty Mn_3Sn diffraction streaks indicating a fast transition to Mn_3Sn but imperfect epitaxial growth. After 3 minutes of deposition, the Mn_3Sn RHEED signatures (Figs. 4(g,h)) become even more spotty alongside the disappearance of some fractional spots seen initially. But the later RHEED patterns, especially those obtained at the final thickness of $\sim$ 200 nm Mn_3Sn, and after cooling down to room temperature ($T_{GS} \sim 19$°C), exhibit well-defined streaky streaks along both azimuths (Figs. 4(i,j)). Overall, the RHEED streak patterns demonstrate a transition from an initial 3D growth mode to a 2D epitaxial growth mode in the later stages of growth, for Mn_3Sn on *c*-plane GaN, while maintaining lattice coherence across the 2 heterointerfaces and with the final epitaxial orientation relationships as follows:

$[11\bar{2}0]_{Mn_3Sn} \parallel [10\bar{1}0]_{GaN} \parallel [11\bar{2}0]_{Al_2O_3}$

$[10\bar{1}0]_{Mn_3Sn} \parallel [11\bar{2}0]_{GaN} \parallel [10\bar{1}0]_{Al_2O_3}$

$[0001]_{Mn_3Sn} \parallel [000\bar{1}]_{GaN} \parallel [0001]_{Al_2O_3}$

A comparative RHEED analysis of the final Mn_3Sn streak pattern with the GaN streak pattern at 300K is presented in Fig. 5. The GaN surface exhibits well-defined RHEED streaks along $[10\bar{1}0]$ (Fig. 5(a) and $[11\bar{2}0]$ Fig. 5(b)), and the first-order diffraction streaks are delineated by dark blue dashed lines. (Note the weak 5× reconstruction streaks just visible in the $[10\bar{1}0]$ streak pattern (Fig. 5(a)); this may correspond to the Ga-polar 5×5 reconstruction as reported by Smith *et al.*;[31] MBE growth on nitridated Al_2O_3 is expected to give N-polarity, but Ga-polarity or mixed polarity could be caused by impurities.) The final Mn_3Sn surface exhibits sharp and regularly spaced first-order diffraction streaks which are marked by dashed magenta lines. It can be seen that the Mn_3Sn lines lie inside the GaN lines (smaller k-value), corresponding to the a for Mn_3Sn being $\sim$ 2.5% larger than $\sqrt{3}a$ for GaN (5.524 Å). Using the GaN streak spacings for calibration, the *in-plane* lattice parameters of Mn_3Sn are measured to be 5.655 Å along $[11\bar{2}0]$ and 5.673 Å along $[10\bar{1}0]$. These numbers differ by only 0.32%, and their average (5.664 Å) differs by only -0.018%

from the accepted Mn_3Sn bulk c-plane value (a = 5.665 Å),[2, 4, 9] excellent agreement. The 0.32% difference between $11\bar{2}0$ and $10\bar{1}0$, and especially the -0.018% difference between the average and expected, are well within our RHEED system precision of $\sim$ 0.43%[32] and can be attributed to statistical error. Therefore, we cannot detect any *in-plane* strain.

Another check we can do of the crystalline symmetry of the surface is to examine the full azimuthal RHEED map. Shown in Fig. 6 is the azimuthal map of the Mn_3Sn surface with full 360° rotational viewing. It is seen that there are just 2 characteristic patterns - $[11\bar{2}0]$ and $[10\bar{1}0]$ - which alternate every 30°. The patterns consistently show streaky streaks all around in every direction. (Note there are 2 blocked beam directions where we could not get a pattern.) The azimuthal symmetry is indicative of a high quality Weyl semimetal surface. The streaks indicate the surface is very smooth, in fact atomically smooth, and having the c-plane crystalline structure.

Figure 7 shows the XRD pattern of the Mn_3Sn/GaN/Al_2O_3 (0001) heterostructure film. Three strong peaks, and a variety of tiny unknown peaks (u.p.'s), are clearly seen. The four largest peaks, including the Al_2O_3, GaN, and Mn_3Sn peaks plus u.p.4 to the left of the Mn_3Sn peak, were fit with Pseudo-Voigt fitting functions in order to extract peak centroids and peak widths. The spectrum was first calibrated by setting the Al_2O_3 0006 peak to be precisely at 41.720°, corresponding to an interplanar spacing of 2.165 Å ($c = 6d = 12.992$ Å) in agreement with best accepted values for Al_2O_3.[14, 15]. After this, the GaN 0002 peak is seen at the angle 34.575° corresponding to an interplanar spacing of 2.594 Å ($c = 5.189$ Å) which differs by only +0.077% from the well known accepted value (5.185 Å).[33] And then the most prominent peak in the whole spectrum, the Mn_3Sn 0002 peak, is seen at angle 39.810° corresponding to an interplanar spacing of 2.265 Å ($c = 4.529$ Å). This differs from the expected value ($c = 4.531$ Å)[2, 4, 9] by only -0.044%, much less than our estimated peak uncertainty (σ) of 0.57%, and therefore we cannot detect any *out-of-plane* strain.

The widths of the 3 main XRD peaks are characterized in terms of their FWHM values which, for Mn_3Sn, GaN, and Al_2O_3 , were calculated from the results of the Pseudo-Voigt fitting using the Thompson-Cox-Hastings formula, resulting in $\text{FWHM}_{Mn3Sn} = 0.56°$, $\text{FWHM}_{GaN} = 0.54°$, and $\text{FWHM}_{Al2O3} = 0.47°$. We see that the Mn_3Sn peak is almost as sharp as the GaN peak which is only a little less sharp compared to the Al_2O_3 peak.

Unknown peaks present in the XRD spectrum include: u.p.1) a tiny peak near 31.1° which might correspond to a strained Mn_3Sn $11\bar{2}0$ ideally expected at 31.59°; u.p.2) a tiny peak near 35.8° which does not quite match the position for Mn_3Sn $20\bar{2}0$ expected at 36.64°; u.p.3) a tiny peak near 37.5°; and u.p.4) a small and wide peak at 39.02° which could correspond to a strained Mn_2Sn $11\bar{2}0$ expected at 40.00° corresponding to the lattice constant 4.508 Å as given in the Mn_2Sn dataset from the Materials Project.[34] Aside from these residual phase/orientations, the large amplitude of the primary Mn_3Sn 0002 peak shows that the film has predominant Mn_3Sn (0001) crystallinity.

In fact, if we assume that the peak at 39.02° does correspond to Mn_2Sn, then the peak amplitudes can be used to estimate volume fractions for Mn_3Sn and Mn_2Sn. The results from the Pseudo-Voigt peak fitting then give Mn_3Sn fraction = 81.5% and Mn_2Sn fraction = 18.5%. These numbers can be compared to the RBS results.

At 5.5 MeV incident beam particle energy, the RBS spectrum was obtained, as seen in Fig. 8(a), in which the peaks are sufficiently separated to measure the number of counts in each peak. The numbers of counts were determined by numerical integration after background subtraction. The results were used to determine the ratio of Mn:Sn for the film as a whole which works out to 2.85:1 ± 4%, with the error estimate based on $\sqrt{N}$ statistics. We can use the volume fractions estimated from XRD to determine a weighted Mn:Sn ratio using the following formula:

$$Mn : Sn = (3 : 1) f_{Mn3Sn} + (2 : 1) f_{Mn2Sn} \tag{1}$$

Using the XRD derived fractions (81.5% Mn_3Sn and 18.5% Mn_2Sn), we estimate the Mn:Sn overall ratio in the film to be 2.82:1 which compares very well with the RBS overall ratio 2.85:1.

The ratio of Ga:Sn was determined to be 1.08:1 with an uncertainty of $\sim$ 4%. Using these ratios, the 2.2 MeV incident beam energy RBS spectrum can be compared to a simulated RBS spectrum using the RUMP software.[16] Although it is not possible to simulate this sample in detail, the deviation from the spectrum for an ideal layered sample structure indicates a 3-dimensional morphology. Combining the information from the 2.2 and 5.5 MeV spectra, it is possible to calculate the total Mn, Sn, and GaN contents of the sample, and we find areal densities of $\sigma_{Mn} = 9.00 \times 10^{17}$ atoms/cm^2, $\sigma_{Sn} = 3.16 \times 10^{17}$ atoms/cm^2, and $\sigma_{GaN} = 3.57 \times 10^{17}$ GaN molecules/cm^2, respectively. Assuming lattice constant values as measured from RHEED and XRD for the sample, these areal density numbers yield GaN and Mn_3Sn layer thicknesses of 81.1 nm and 198.8 nm, respectively.

Using AFM, we have imaged the Mn_3Sn sample surface, and the images shown in Fig. 9(a,b) reveal a mesa-valley growth morphology. The individual mesas suggest micro-crystalline growth structures with highly aligned crystalline orientations. Line sections are plotted in Fig. 9(c-e) with successively smaller lengths. The line sections in Fig. 9(c,d) show the steep sides of the mesa structures, extending from presumably the GaN surface to the mesa tops, but also their smooth tops. The line section in Fig. 9(e) shows the nanometer-scale flatness of the mesa tops, suggesting that the mesa tops are atomically smooth. Although overall the film has large rms roughness (44 nm) on account of the mesa-valley morphology, not only do the micro-crystallites have typically very flat mesa tops, but also their *in-plane* shapes reflect the hexagonal *in-plane* crystalline structure of $Mn_3Sn(0001)$. For example, one cay see clearly hexagonal side edges with 3 characteristic edge directions, opposite edges being parallel to each other, as indicated in Fig. 9(f). This indicates that the mesa structures have highly *in-plane* and *out-of-plane* crystalline alignments.

A zoom-in to one of the flat Mn_3Sn (0001) mesa tops was acquired with UHV-STM showing an atomically smooth surface with atomic height steps as seen in Fig. 10(a). This image was acquired in constant tunneling current mode. One sees in the image an atomically flat region at the top terrace together with atomic steps running from upper left to lower middle of the image area. As indicated by the line profile displayed in Fig. 10(b), the heights of the steps are consistent with monolayers of Mn_3Sn of height $c/2$ (2.264 Å).

The implications of the observed morphology as revealed by AFM and *in-situ* UHV-STM are that while the Mn_3Sn (0001) on c-plane w-GaN grows epitaxially smoothly in the later stages of growth, there exists at the onset of growth a low density of Mn_3Sn (0001) nucleation sites rather than a uniform nucleation layer, leading to the formation of the mesa-valley morphology we see. This implies the existence of epitaxial columnar growth which is characterized by discreet, well-aligned crystalline islands, atomically-smooth mesa tops, but deep valleys indicating a lack of island coalescence.[35] In our case, the (0001) Mn_3Sn surface is energetically favorable as evidenced by the atomically smooth AFM and STM images of the mesa tops suggesting high surface atom diffusion. To further improve the overall film morphology, we would need to do further growth studies aimed at inducing a much higher density of nucleation sites, possibly using a low-temperature buffer layer method.

IV. CONCLUSIONS AND OUTLOOK

It can be concluded that the growth procedures used here result in epitaxial columnar growth of Weyl semimetal $Mn_3Sn(0001)$ thin films with smooth mesa-top surfaces, showing that wurtzite GaN/Al_2O_3 (0001) is an ideal substrate for the growth of Mn_3Sn (0001). The measured lattice constants for the Mn_3Sn thin film (a = 5.664 Å and c = 4.529 Å are in excellent agreement with expected relaxed values (−0.018% diff *in-plane* and −0.044% diff *out-of-plane*, respectively), with the differences being smaller than the measurement uncertainties. Consequently, we cannot determine that any strain exists in these films prepared in this way. These results are very good and show outstanding promise for both spintronic applications and fundamental properties studies including surface investigations of pristine Mn_3Sn (0001) surfaces.

The open questions remaining include a) whether or not there is any causal relationship between the observed epitaxial columnar growth mode and the strain-free film; b) what are the detailed atomic models for the interfaces between Mn_3Sn (0001) and c-plane wurtzite GaN; and c) how to achieve closer to 100% phase purity. As the RBS data suggests that the sample overall is Mn-poor with respect to an ideal 3:1 stoichiometry, therefore a higher Mn flux during growth could potentially improve the phase purity. And more work should be done to clearly determine the effect of wurtzite GaN lattice polarity on the growth of Mn_3Sn (0001) layers.

V. ACKNOWLEDGMENTS

The authors acknowledge support from the U.S. Department of Energy, Office of Basic Energy Sciences, Division of Materials Sciences and Engineering under Award No. DE-FG02-06ER46317. The authors would like to thank Dr. Eric Stinaff and his students for back-coating the sapphire substrates and for the use of their atomic force microscope. The authors would like to thank Mr. Greg Secord from Fluke Process Instruments for help with the optical pyrometer measurements using the Fluke pyrometer model E2MH-F0-V-0-0 and in carrying out the sample temperature calibration.

VI. DATA AVAILABILITY

The data supporting this study's findings are openly available in Zenodo at: 10.5281/zenodo.17552646.

VII. DECLARATION OF GENERATIVE AI AND AI-ASSISTED TECHNOLOGIES IN THE MANUSCRIPT PREPARATION PROCESS

During the preparation of this work, the authors used Microsoft Copilot in order to search for some of the references and to format the references in AIP style. Copilot was also used to search for scientific information including methods. Copilot was not used to draft any portions of the manuscript nor to revise the manuscript. After using this tool/service, the authors reviewed and edited the content as needed and take full responsibility for the content of the published article.

[1] H. Yang, Y. Sun, Y. Zhang, W.-J. Shi, S. S. P. Parkin, and B. Yan, "Topological Weyl semimetals in the chiral antiferromagnetic materials Mn_3Ge and Mn_3Sn," *New J. Phys.* **19**, 015008 (2017).

[2] S. Nakatsuji, N. Kiyohara, and T. Higo, "Large anomalous Hall effect in a non-collinear antiferromagnet at room temperature," *Nature* **527**, 212 (2015).

[3] T. Higo, D. Qu, Y. Li, C. L. Chien, Y. Otani, and S. Nakatsuji, "Anomalous Hall effect in thin films of the Weyl antiferromagnet Mn_3Sn," *Appl. Phys. Lett.* **113**, 202402 (2018).

[4] T. Tomita, M. Ikhlas, and S. Nakatsuji, "Large Nernst effect and thermodynamics properties in Weyl antiferromagnet," *JPS Conf. Proc.* **30**, 011009 (2020).

[5] T. Higo, H. Man, D. B. Gopman, L. Wu, T. Koretsune, O. T. E. Van, Y. P. Kabanov, D. Rees, Y. Li, M. T. Suzuki, S. Patankar, M. Ikhlas, C. L. Chien, R. Arita, R. D. Shull, J. Orenstein, and S. Nakatsuji, "Large magneto-optical Kerr effect and imaging of magnetic octupole domains in an antiferromagnetic metal," *Nat. Photonics* **12**, 73 (2018).

[6] M. Kimata, H. Chen, K. Kondou, S. Sugimoto, P. K. Muduli, M. Ikhlas, Y. Omori, T. Tomita, A. H. MacDonald, S. Nakatsuji, and Y. Otani, "Magnetic and magnetic inverse spin Hall effects in a non-collinear antiferromagnet," *Nature* **565**, 627 (2019).

[7] X. F. Zhou, X. Z. Chen, Y. F. You, L. Y. Liao, H. Bai, R. Q. Zhang, Y. J. Zhou, H. Q. Wu, C. Song, and F. Pan, "Exchange bias in antiferromagnetic Mn_3Sn monolayer films," *Phys. Rev. Appl.* **14**, 054037 (2020).

[8] S. Tomiyoshi, and Y. Yamaguchi, "Magnetic structure and weak ferromagnetism of Mn_3Sn studied by polarized neutron diffraction," *J. Phys. Soc. Jpn* **51**, 2478 (1982).

[9] T. Higo, K. Kondou, T. Nomoto, M. Shiga, S. Sakamoto, X. Chen, D. Nishio-Hamane, R. Arita, Y. Otani, S. Miwa, and S. Nakatsuji, "Perpendicular full switching of chiral antiferromagnetic order by current," *Nature* **607**, 474 (2022).

[10] J. Y. Yoon, P. Zhang, C. T. Chou, *et al.*, "Handedness anomaly in a non-collinear antiferromagnet under spin–orbit torque," Nat. Mater. **22**, 1106 (2023)..

[11] J. Liu, Z. Zhang, M. Fu, X. Zhao, R. Xie, Q. Cao, and L. Bai, "The anomalous Hall effect controlled by residual epitaxial strain in antiferromagnetic Weyl semimetal Mn_3Sn thin films grown by molecular beam epitaxy," *Results Phys.* **52**, 106803 (2023).

[12] S. Upadhyay, T. Erickson, H. Hall, A. Shrestha, D. C. Ingram, K. Sun, J. C. M. Hernandez, G. H. Cocoletzi, N. Takeuchi, and A. R. Smith, "Exploring the interfacial structure and crystallinity for direct growth of $Mn_3Sn(0001)$ on sapphire (0001) by molecular beam epitaxy," *Surf. Interfaces* **42**, 103379 (2023).

[13] S. Upadhyay, T. Erickson, H. Hall, A. Shrestha, D. C. Ingram, K. Sun, J. C. Moreno Hernandez, G. H. Cocoletzi, N. Takeuchi, and A. R. Smith, "Molecular beam epitaxy and crystal structure of majority a-plane-oriented and substrate-strained Mn_3Sn thin films grown directly on sapphire (0001)," *J. Vac. Sci. Technol. A* **41**, 042710 (2023).

[14] Yu. V. Shvyd'ko, M. Lucht, E. Gerdau, M. Lerche, E. E. Alp, W. Sturhahn, J. Sutter, and T. S. Toellner, "Measuring wavelengths and lattice constants with the Mössbauer wavelength standard," *J. Synchrotron Rad.* **9**, 17 (2002).

[15] M. Lucht, M. Lerche, H.-C. Wille, Yu. V. Shvyd'ko, H. D. Rüter, E. Gerdau, and P. Becker, "Precise Measurement of the Lattice Parameters of Sapphire in the Temperature Range 4.5 K - 250 K Using the Mössbauer Wavelength Standard," *J. Appl. Cryst.* **36**, 1075 (2003).

[16] L. R. Doolittle, "Algorithms for the rapid simulation of Rutherford backscattering spectra," Nucl. Instrum. Methods Phys. Res. B **9**, 344–351 (1985). https://doi.org/10.1016/0168-583X(85)90762-1.

[17] I. Horcas, R. Fernández, J. M. Gomez-Rodriguez, J. Colchero, J. Gómez-Herrero, and A. M. Baro, "WSXM: A software for scanning probe microscopy and a tool for nanotechnology," Rev. Sci. Instrum. **78**, 013705 (2007). https://doi.org/10.1063/1.2432410.

[18] J. Chiang, D. P. Birnie III, and W. D. Kingery, *Physical Ceramics* (Wiley, MIT, 1997).

[19] E. R. Dobrovinskaya, L. A. Lytvynov, and V. Pishchik, *Properties of Sapphire* (Springer Nature, 2009), pp. 55–176.

[20] K. Fujiwara, A. Ishii, T. Ebisuzaki, T Abe, and K. Ando, "Theoretical Investigation on the Structural Properties of ZnO Grown on Sapphire," e-J. Surf. Sci. Nanotech **4**, 544 (2006).

[21] W. A. Melton and J. I. Pankove, "GaN growth on sapphire," J. Cryst. Growth **178**, 168–173 (1997).

[22] J.-S. Paek, K.-K. Kim, J.-M. Lee, D.-J. Kim, M.-S. Yi, D. Y. Noh, H.-G. Kim, and S.-J. Park, "Nitridation of sapphire substrate and its effect on the growth of GaN layer at low temperature," J. Cryst. Growth **200**, 55 (1999).

[23] A. Yamamoto, M. Tsujino, M. Ohkubo, and A. Hashimoto, “Nitridation effects of substrate surface on the metalorganic chemical vapor deposition growth of InN on Si and α-Al_2O_3 substrates,” J. Cryst. Growth **137**, 415–420 (1994).

[24] C. Heinlein, J. Grepstad, H. Riechert, and R. Averbeck, “Plasma preconditioning of sapphire substrate for GaN epitaxy,” Mater. Sci. Eng. B **43**, 253–257 (1997).

[25] A. Kikuchi, H. Hoshi, and K. Kishino, “Substrate nitridation effects on GaN grown on GaAs substrates by molecular beam epitaxy using RF-radical nitrogen source,” Jpn. J. Appl. Phys. **33**, 688 (1994).

[26] T. D. Moustakas, T. Lei, and R. J. Molnar, “Growth of GaN by ECR-assisted MBE,” Physica B **185**, 36–49 (1993).

[27] H. Kawakami, K. Sakurai, K. Tsubouchi, and N. Mikoshiba, “Epitaxial growth of AlN film with an initial-nitriding layer on α-Al_2O_3 substrate,” Jpn. J. Appl. Phys. **27**, L161 (1988).

[28] J. I. Hütner, A. Conti, D. Kugler, F. Mittendorfer, G. Kresse, M. Schmid, U. Diebold, and J. Balajka, “Stoichiometric reconstruction of the Al_2O_3 (0001) surface,” Science **385**, 1241–1244 (2024).

[29] S. Smink, L. N. Majer, H. Boschker, J. Mannhart, and W. Braun, “Long-Range Atomic Order on Double-Stepped Al_2O_3(0001) Surfaces,” Adv. Materials **36**, 2312899 (2024).

[30] D. Nilsson, E. Janzén, and A. Kakanakova-Georgieva, “Lattice parameters of AlN bulk, homoepitaxial and heteroepitaxial material,” J. Phys. D: Appl. Phys. **49**, 175108 (2016).

[31] A. R. Smith, R. M. Feenstra, D. W. Greve, M.-S. Shin, M. Skowronski, J. Neugebauer, and J. E. Northrup, “GaN(0001) surface structures studied using scanning tunneling microscopy and first-principles total energy calculations,” Surf. Sci. **423**, 70 (1999).

[32] A. Abbas, J. C. Moreno Hernandez, A. Shrestha, D. Russell, T. Erickson, K. Sun, G. Hernandez Cocoletzi, F. Yang, and A. R. Smith, “Experimental and theoretical investigation of the crystalline surface, film, and interface properties of antiperovskite Mn_3GaN grown by molecular beam epitaxy on MgO(001),” Surf. Interfaces **64**, 106201 (2025).

[33] Argonne National Laboratory, “Crystal Lattice Parameters,” available at https://7id.xray.aps.anl.gov/calculators/crystal_lattice_parameters.html, accessed 6 November 2025.

[34] Materials Project, “mp-22514: Mn_2Sn (hexagonal, $P6_3/mmc$, 194),” Materials Project, https://legacy.materialsproject.org/materials/mp-22514/, accessed November 6,

2025.

[35] G. Ferro, "Epitaxial growth of thin films," MTI Japan, available at https://mti-japan.com/wp-content/uploads/2014/07/Epitaxial-growth-of-thin-film.pdf, accessed 6 November 2025.

FIGURES

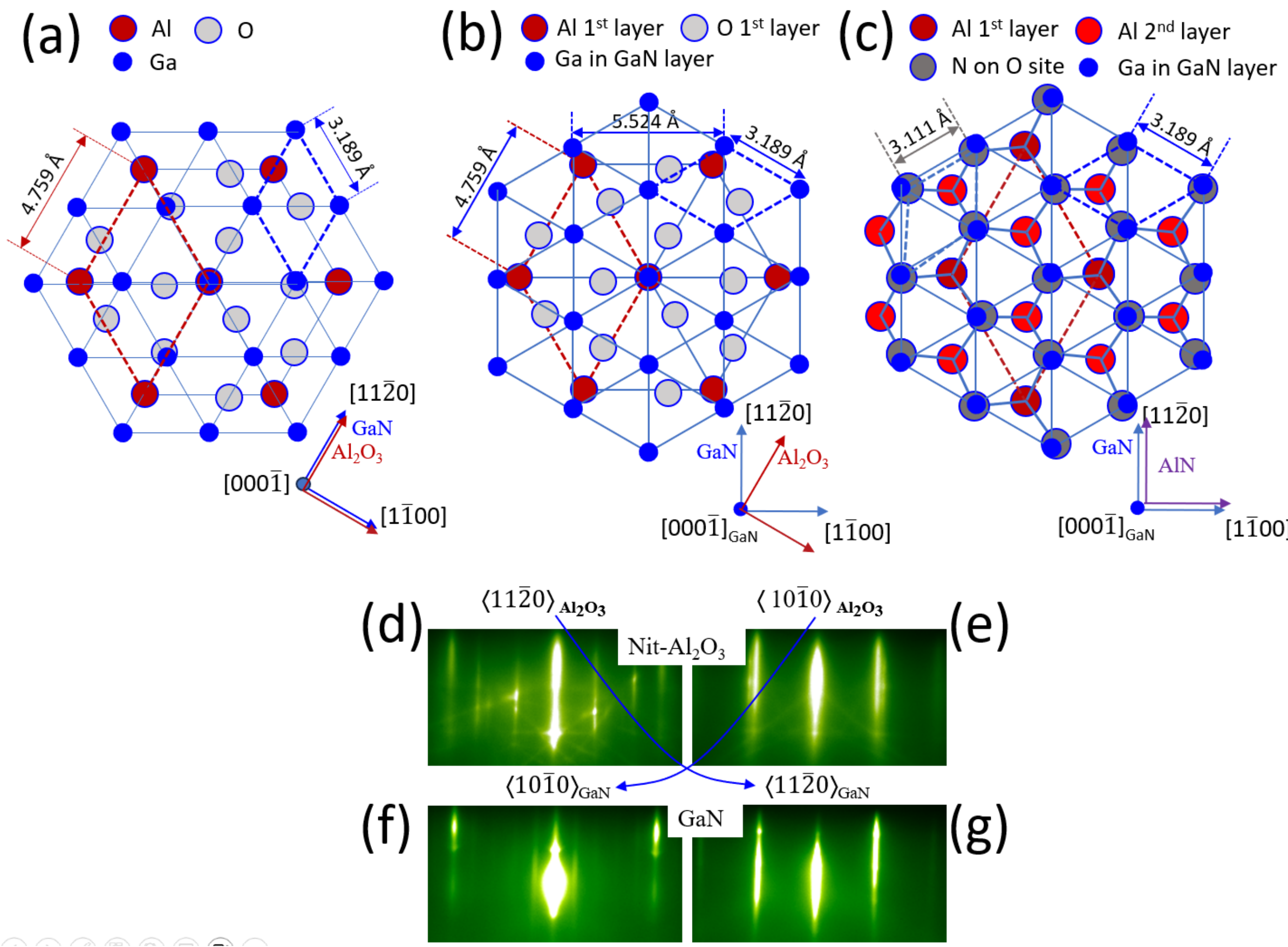

FIG. 1. Modeling GaN growth on sapphire (a) without nitridation and (b) with nitridation of sapphire surface. (a) GaN lattice ($a_{\mathrm{GaN}(0001)} = 3.189$ Å) on sapphire lattice ($a_{\mathrm{Al_2O_3}(0001)} = 4.759$ Å), illustrating a lattice mismatch of -33.0%; sapphire and GaN surface unit cells are shown by dashed lines. Only 1st layer Al sites are shown to indicate the surface unit cell lattice of Al_2O_3; the O sublattice is 30° misaligned to the Al sublattice as well as with the Ga (of GaN) sublattice overlaid; (b) GaN(000$\bar{1}$) lattice rotated 30° on Al_2O_3 (0001) reduces the lattice mismatch to $+16.0\%$ with $a_{Al_2O_3(0001)} = 4.759$ Å and $\sqrt{3}\, a_{\mathrm{GaN}(0001)} = 5.524$ Å; sapphire and GaN surface unit cells are shown by dashed lines; (c) after rf plasma nitridation of the Al_2O_3 substrate surface, illustrating the formation of an AlN-like surface and subsequent reduction of lattice mismatch to $+2.49\%$ with $a_{\mathrm{AlN}(0001)} = 3.111$ Å; both 1st and 2nd layer Al atom are shown as well as N atoms on O sites; sapphire, AlN, and GaN surface unit cells are shown by dashed lines; (d,e) RHEED patterns of nitridated Al_2O_3 surface before GaN growth; and (f,g) RHEED patterns along the same beam directions after GaN growth.

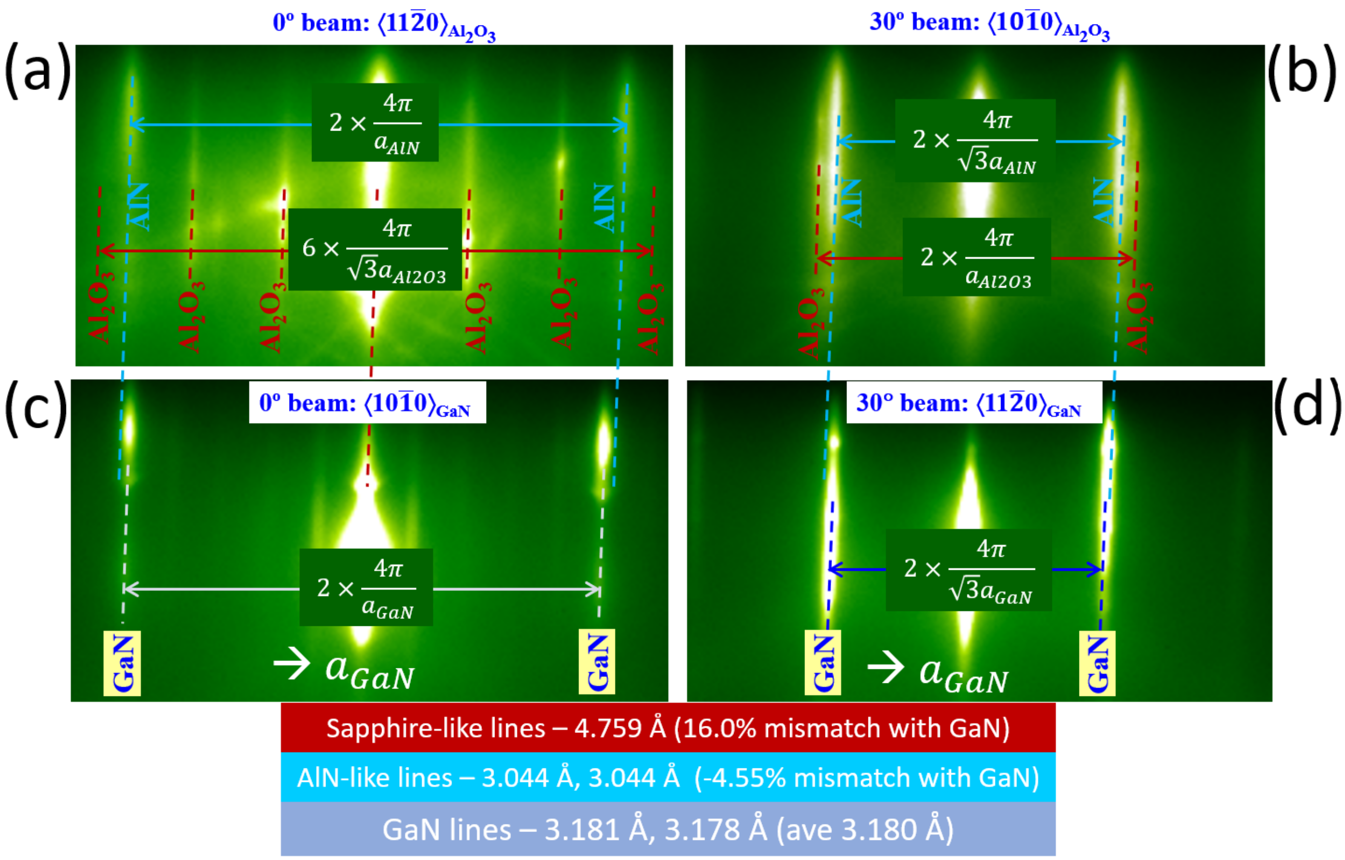

FIG. 2. RHEED patterns before (a,b) and after (c,d) GaN growth on nitridated Al_2O_3 (0001). (a,b) RHEED shows 1st-order primary streaks corresponding to original Al_2O_3 (0001) (red dashed lines) lattice but also 1st-order AlN-like streaks (cyan dashed lines) indicating a 30° lattice rotation; (c,d) overgrown GaN RHEED streaks slightly closer together compared to the AlN streaks. Reciprocal lattice streak spacings given in terms of inverse lattice constants.

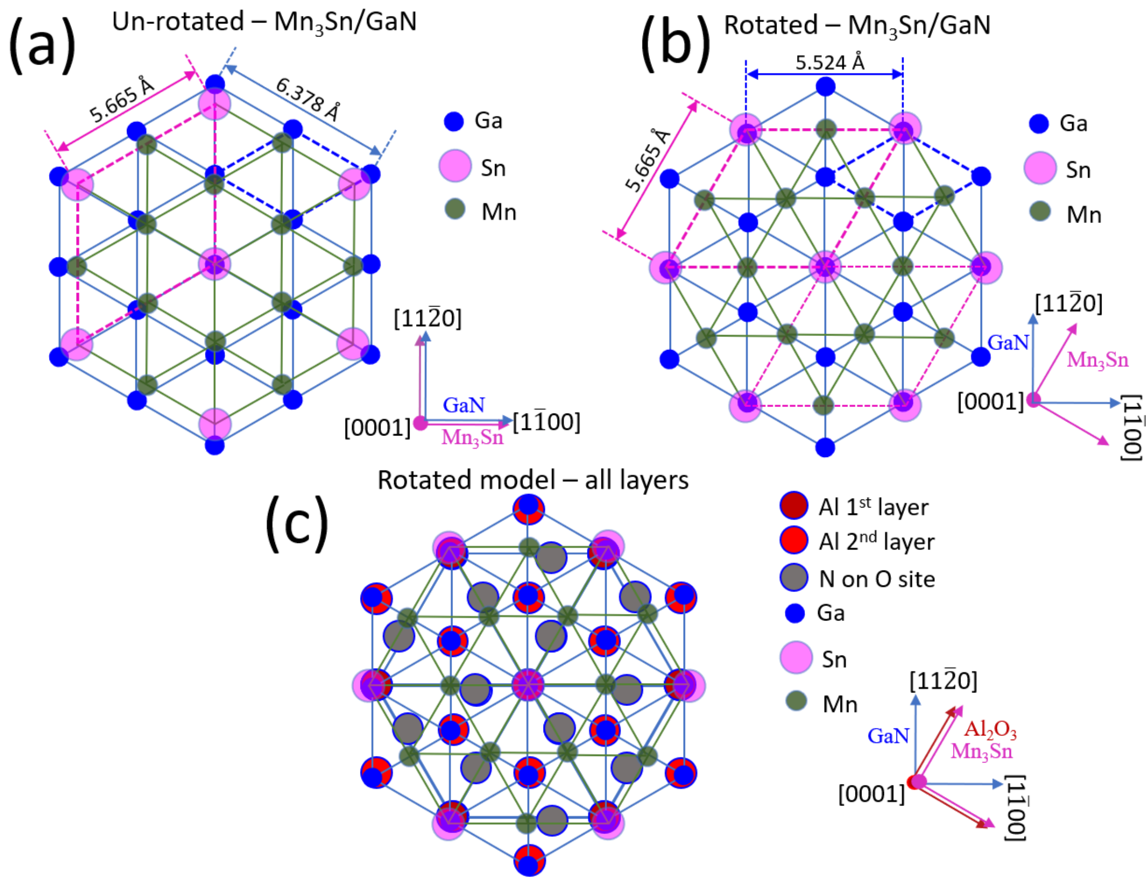

FIG. 3. Growth schematic of Mn_3Sn (0001) on c-plane GaN with (a) *in-plane* axes aligned resulting in -11.2% lattice mismatch with $a_{\mathrm{Mn_3Sn(0001)}} = 5.665$ Å and $2 \times a_{\mathrm{GaN(0001)}} = 2 \times 3.189$ Å $= 6.378$ Å; GaN and Mn_3Sn surface unit cells are shown by dashed lines; (b) With *in-plane* 30° rotation on c-plane GaN, reducing the lattice mismatch to $+2.63\%$; GaN and Mn_3Sn surface unit cells are shown by dashed lines; (c) combined schematic lattice overlay of c-plane Mn_3Sn on GaN on nitridated sapphire.

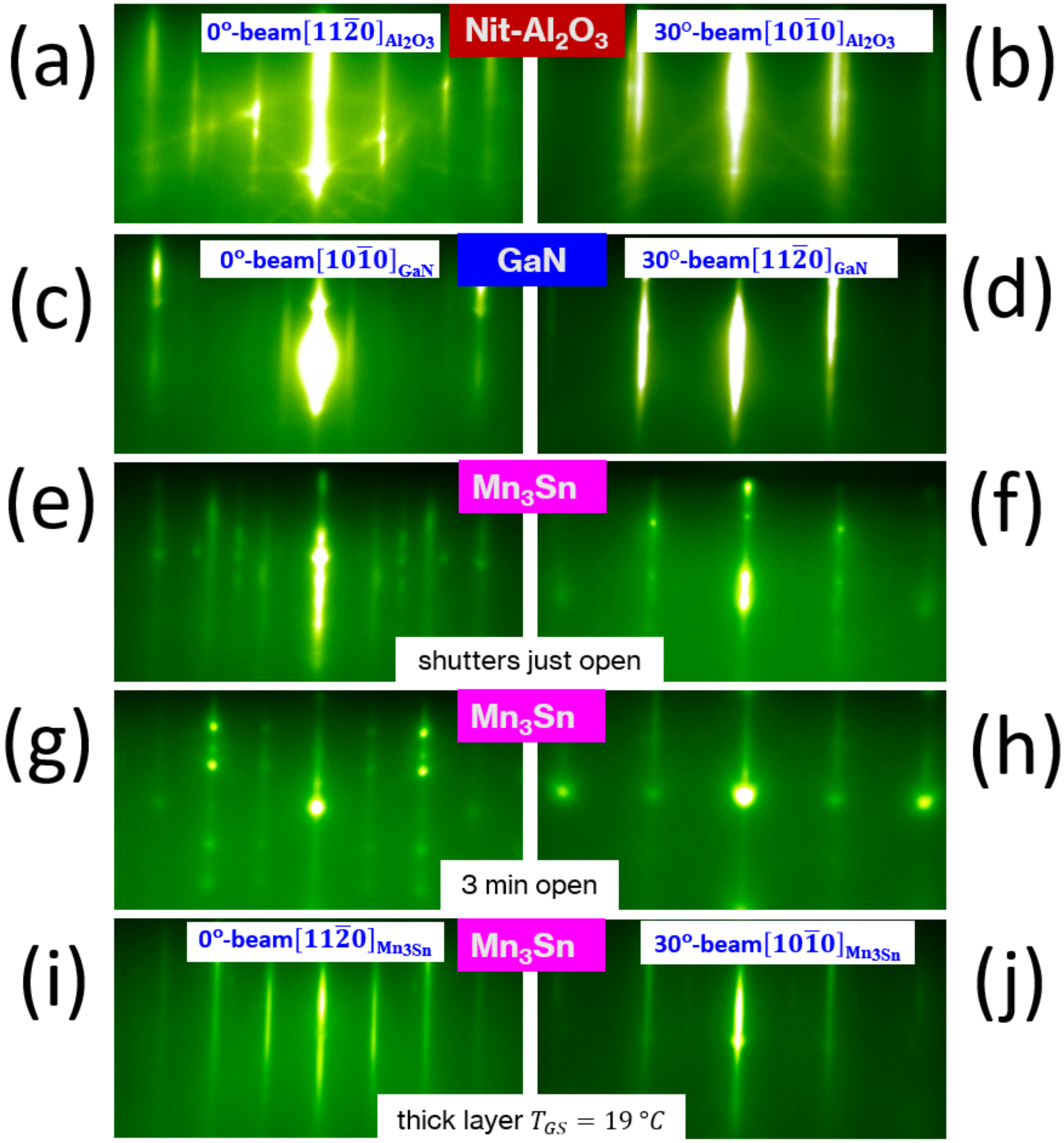

FIG. 4. RHEED patterns captured during epitaxial growth of Mn_3Sn (0001) on *c*-plane GaN on Al_2O_3 (0001): (a,b) nitridated Al_2O_3 substrate; (c,d) GaN after growth of a thick layer; (e–h) Mn_3Sn during the initial stages of growth; (i,j) Mn_3Sn after growth of a thick layer and cooling to room temperature.

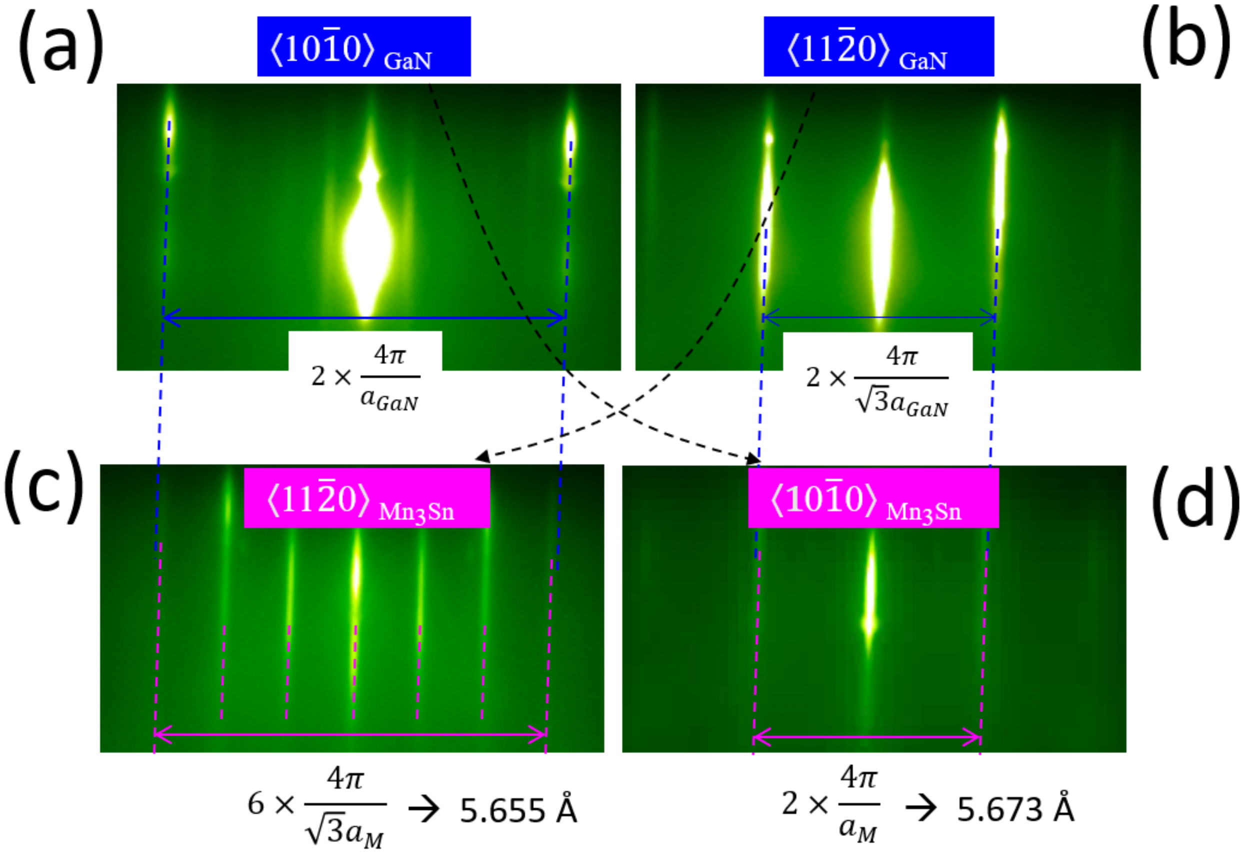

FIG. 5. RHEED patterns of c-plane GaN and Mn_3Sn films along different azimuths. (a,b) RHEED patterns of c-plane GaN before the growth of Mn_3Sn; (c,d) RHEED patterns after the completed growth of Mn_3Sn, where it is observed that the crystal lattice vector directions have interchanged. Measured *in-plane* lattice spacings are indicated.

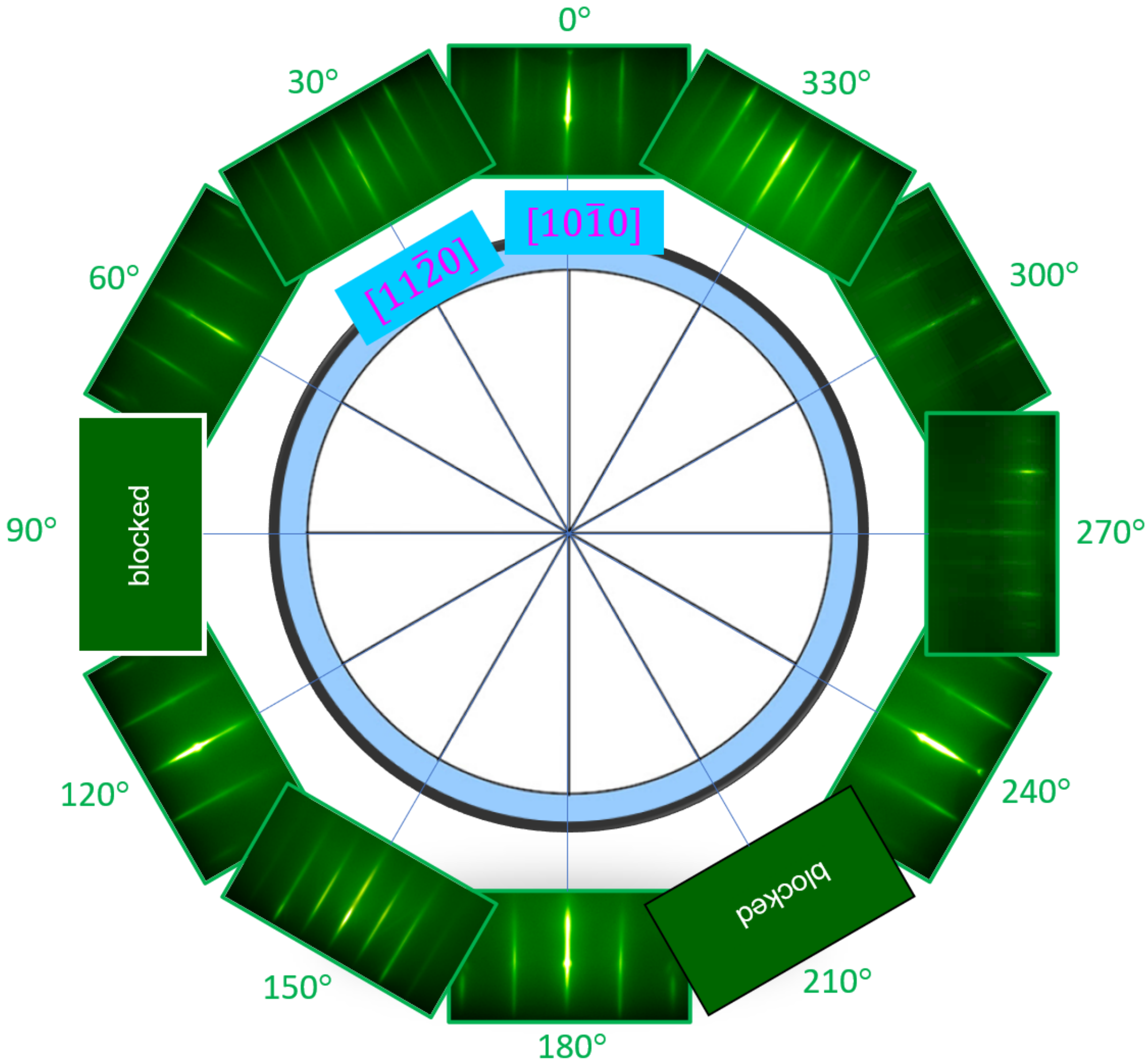

FIG. 6. 360° RHEED azimuth map for Mn_3Sn (0001). The patterns exhibit well-defined streaks, indicative of a well-ordered crystalline surface. A clear six-fold rotational symmetry is observed, consistent with the hexagonal crystal structure of Mn_3Sn. The primary crystallographic orientations, [11$\bar{2}$0] and [10$\bar{1}$0], are marked for reference. The 90° and 210° azimuths are blocked by the sample holder clips.

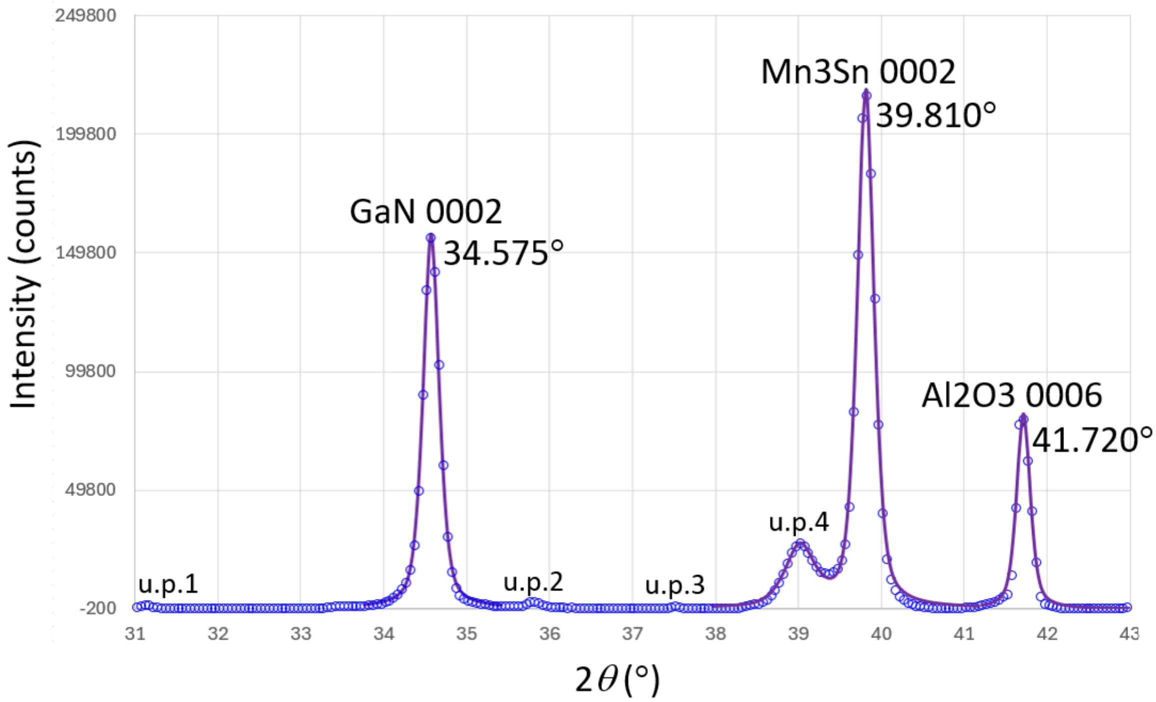

FIG. 7. X-ray diffraction pattern of Mn_3Sn/c-plane GaN/Al_2O_3. The primary peaks seen are the 0002 for Mn_3Sn (magenta label), the 0002 for GaN (blue label), and the 0006 for Al_2O_3 (black label). A small $11\bar{2}0$ peak for Mn_2Sn is also seen along with very small $11\bar{2}0$ and $20\bar{2}0$ Mn_3Sn peaks. One other peak near 37.5° is unidentified (Note the log scale).

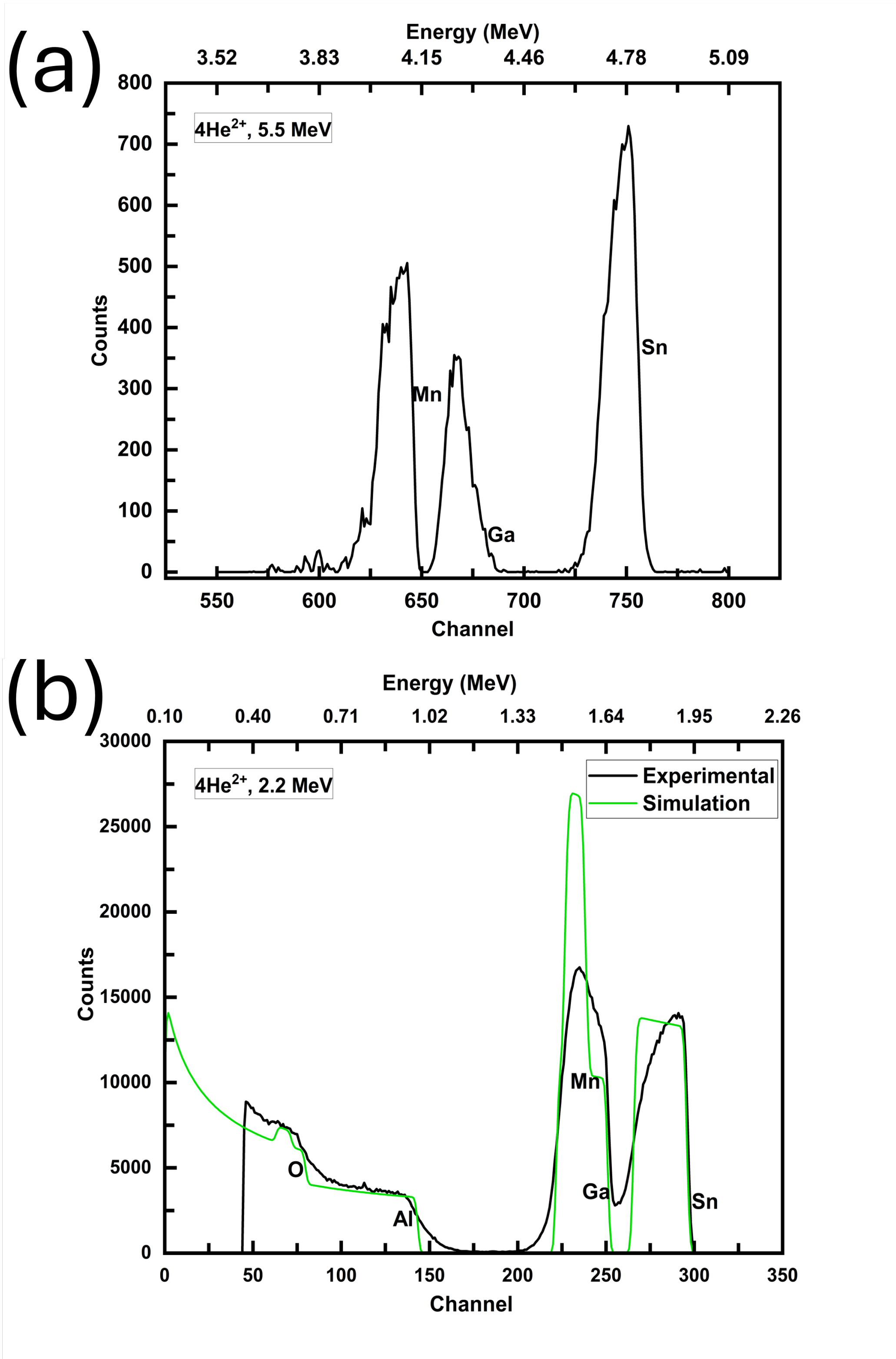

FIG. 8. (a) RBS data at 5.5 MeV showing the separated peaks for Mn, Ga, and Sn; (b) RBS data at 2.2 MeV together with a RUMP simulation.

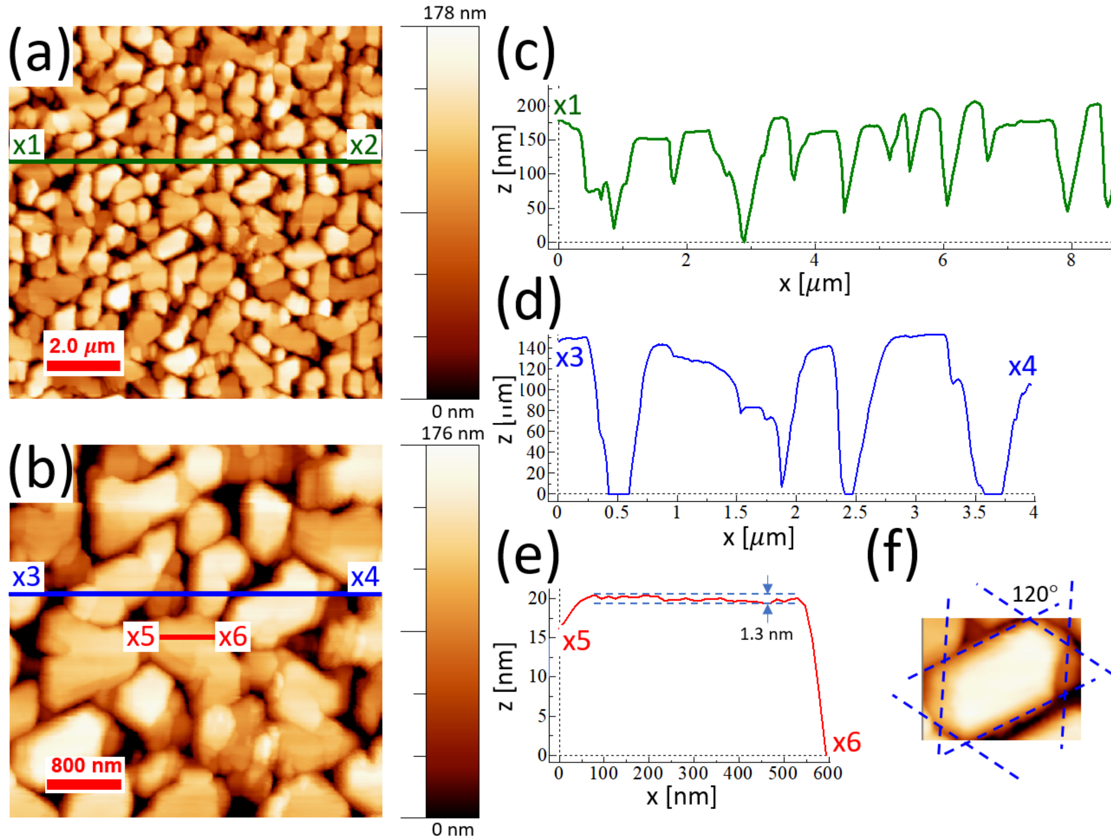

FIG. 9. (a) AFM images acquired *ex-situ* after growth and removing from the MBE chamber. a) 10 micron size image; b) 4 micron size image, zooming in on mesa-valley topography; (c) line profile (green) from x1 to x2, corresponding to profile line (blue) shown from image in (a); (d) line profile (blue) from x3 to x4, corresponding to profile line (blue) from image in (b); (e) line profile (red) from x5 to x6, corresponding to profile line (red) from image in (b); (f) zoom-in view of one mesa top, revealing the 120°-angled side edges of the hexagonal growth structure.

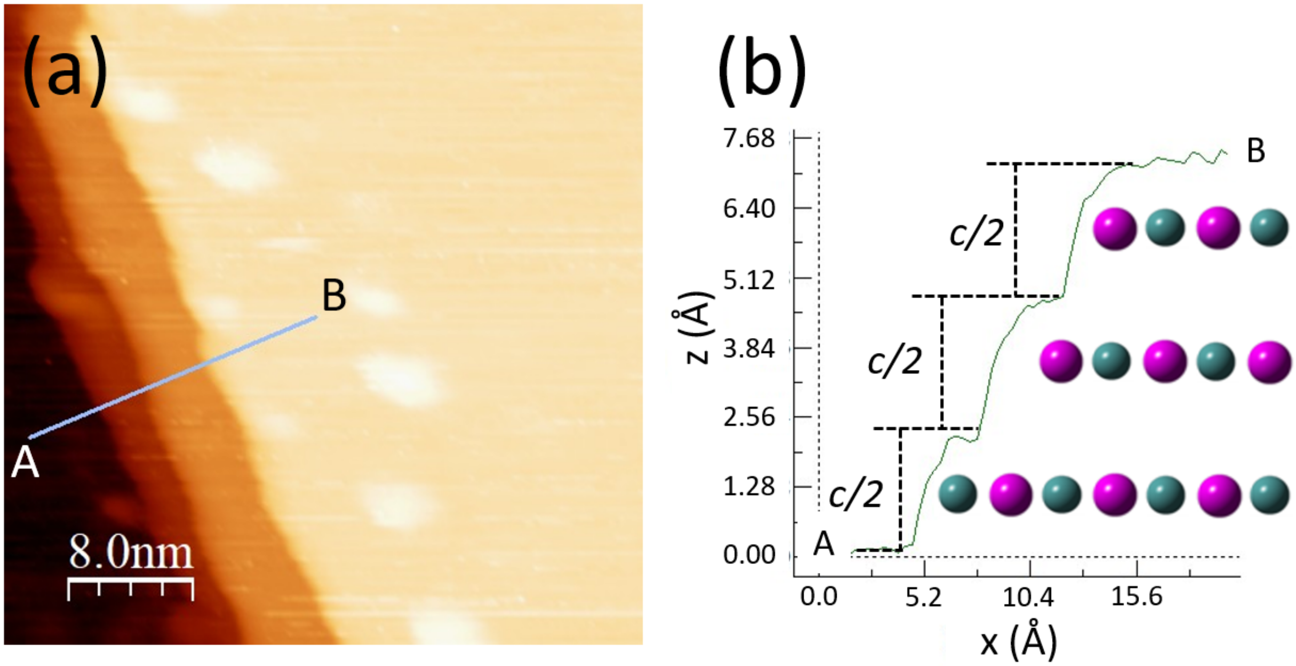

FIG. 10. (a) In-situ UHV-STM image of $Mn_3Sn/GaN/Al_2O_3$ showing atomically smooth terraces and atomic layer height steps. The cross-section line profile A-B at the gray line is displayed in (b); model atoms are not to scale.